

Supporting Information

Homan et al. 10.1073/pnas.1407306111

SI Methods

Characterization of Reaction Between Dimethyl Sulfate and RNA Nucleobases. Adduct formation between dimethyl sulfate (DMS) (Sigma-Aldrich) and [γ - 32 P]-labeled ATP, CTP, and UTP was performed by adding 10% (vol/vol) DMS (1 μ L; 1.7 M in absolute ethanol) to [γ - 32 P]NTP in 1 \times reaction buffer [9 μ L, 10 mM MgCl₂ and 300 mM sodium cacodylate (pH 7.0)] at 37 °C. Reactions were quenched with an equal volume of neat 2-mercaptoethanol (2ME) after 10, 30, 60, 120, 180, 360, and 900 s. For prequench control reactions, 1.3 M DMS solution [1:2.5 (vol/vol) DMS:ethanol:H₂O] was first added to equal volume neat 2-mercaptoethanol. This mixture (2.8 μ L, 625 mM DMS) was then immediately added to [γ - 32 P]NTP in 7.2 μ L of 1.4 \times reaction buffer [7.2 μ L; 14 mM MgCl₂ and 417 mM sodium cacodylate (pH 7.0)], and the reaction was incubated at 37 °C for 15 min. Quenched reactions were resolved by gel electrophoresis (30% polyacrylamide; 29:1 acrylamide:bisacrylamide; 0.4-mm \times 28.5-cm \times 23-cm gel; 30 W, 45 min) and quantified by phosphorimaging. Data were consistent with a mechanism in which DMS forms adducts at the N1 position of adenosine and N3 position of cytosine and does not react with uridine. The change in pH during DMS adduct formation was followed in reactions without NTP at 37 °C using an Accumant 25 pH meter. Direct measurements of DMS adduct formation with cytosine and adenosine suggest roughly equal reactivities with these two nucleotides (Fig. 2). This observation differs from the widespread view that adenosine reacts more rapidly than does cytosine with DMS. We attribute this misconception to the relatively inefficient ability of N3-methyl cytosine to inhibit reverse transcriptase enzymes.

RNA Constructs. DNA templates for the *Escherichia coli* thiamine pyrophosphate (TPP) riboswitch, *Tetrahymena* group I intron P546 domain, and *Bacillus stearothermophilus* RNase P catalytic domain RNAs, each imbedded within 5' and 3' structure cassette flanking sequences, were generated by PCR (1). RNAs were transcribed in vitro [1 mL; 40 mM Tris (pH 8.0), 10 mM MgCl₂, 10 mM DTT, 2 mM spermidine, 0.01% (vol/vol) Triton X-100, 4% (wt/vol) poly (ethylene) glycol 8000, 2 mM each NTP, 50 μ L PCR-generated template, 0.1 mg/mL T7 RNA polymerase; 37 °C; 4 h] and purified by denaturing polyacrylamide gel electrophoresis (8% polyacrylamide, 7 M urea, 29:1 acrylamide:bisacrylamide, 0.4-mm \times 28.5-cm \times 23-cm gel; 32 W, 1.5 h). RNAs were excised from the gel, recovered by passive elution overnight at 4 °C, and precipitated with ethanol. The purified RNAs were resuspended in 50 μ L 10 mM Tris (pH 7.5), 1 mM EDTA (TE) and stored at -20 °C.

RNA Folding and DMS Modification. RNA structure probing experiments were performed in 10 mM MgCl₂ and 300 mM cacodylate at pH 7.0. RNAs [5 pmol in 5 μ L 5 mM Tris (pH 7.5), 0.5 mM EDTA (1/2 \times TE)] were denatured at 95 °C for 2 min, cooled on ice, treated with 4 μ L 2.5 \times folding buffer [750 mM cacodylate (pH 7.0) and 25 mM MgCl₂], and incubated at 37 °C for 30 min. After folding, the P546 domain and the RNase P catalytic domain RNAs were treated with DMS (1 μ L; 1.7 M in absolute ethanol) and allowed to react at 37 °C for 6 min. No-reagent control reactions were performed with 1 μ L absolute ethanol. Reactions were quenched by the addition of an equal volume of neat 2ME and immediately placed on ice. No-Mg²⁺ experiments were performed identically except that the 2.5 \times folding buffer omitted Mg²⁺. The TPP riboswitch RNA was incubated in folding buffer at 37 °C for 10 min, after which the TPP ligand was added at the desired concentration and samples were incubated at 37 °C for 20 min.

(Note: DMS is a known carcinogen and neat 2ME has a very strong odor. Manipulations involving DMS and 2ME should be performed in a chemical fume hood. Solutions containing DMS should be neutralized with 5 N NaOH. Solutions containing DMS or 2ME should be disposed of as chemical waste.)

Reverse Transcription and Adduct Detection. The reverse transcription and adduct detection strategy was adapted from the SHAPE mutational profiling (MaP) approach (2). After treatment with DMS, RNAs were purified using G-50 spin columns (GE Healthcare). Reverse transcription reactions were performed using SuperScript II reverse transcriptase (Invitrogen) for 3 h at 42 °C [0.5 mM premixed dNTPs, 50 mM Tris HCl (pH 8.0), 75 mM KCl, 6 mM MnCl₂, and 10 mM DTT]. Reactions were desalted with G-50 spin columns (GE Healthcare). Under these conditions (long incubation time, in the presence of Mn²⁺), the reverse transcriptase reads through methyl adducts at the N1 and N3 positions of adenosine and cytosine, respectively, yielding a mutation at the site of the adduct. Double-stranded DNA libraries with adaptors and indices compatible with Illumina-based sequencing were generated by PCR. Resulting libraries were pooled and sequenced with an Illumina MiSeq instrument (500 cycle kit) so that the first sequencing read in paired-end mode covered the RNA sequence of interest. Resulting FASTQ data files were aligned to reference sequences and per-nucleotide mutation rates were calculated using an in-house pipeline (2). Phred scores used to count mutations were required to be ≥ 20 . Representative sequencing and clustering statistics are summarized in Fig. S8.

Measurement of Internucleotide Interactions by Statistical Association Analysis. To detect nucleotide reactivity interdependencies, all possible pairs of nucleotides were subjected to Yates' corrected version of Pearson's χ^2 test of independence versus association (3). Yates' corrected χ^2 statistic was computed as

$$\chi^2_{\text{Yates}} = \frac{N(|ad - bc| - 0.5N)^2}{(a+b)(c+d)(a+c)(b+d)}, \quad [\text{S1}]$$

where $n = (a + b + c + d)$ is the total number of strands in the dataset and a , b , c , and d are defined by the following 2×2 contingency table of the observed numbers of four possible co-occurrences:

	Nucleotide i	
	Not mutated (0)	Mutated (1)
Nucleotide j		
Not mutated (0)	a	b
Mutated (1)	c	d

A pair of nucleotides was taken to have a statistically significant association if $\chi^2_{\text{Yates}} > 20$ ($P < 0.00001$). With this high acceptance threshold for an individual nucleotide pair we expect to make no more than one false-positive determination for RNAs at least up to 500 nt long.

For pairs of nucleotides that passed the χ^2 significance test, the sign and strength of the statistical association was determined by computing Pearson's correlation coefficient, ρ . In the case of two binary variables, ρ is equal to Pearson's measure of association, the phi coefficient. The correlation coefficient and the χ^2 statistic are related:

$$\rho^2 = \chi^2 / N. \quad [S2]$$

Although correlation coefficients were typically less than 0.05, coefficients were highly significant. Based on χ^2 statistics, the probability that identified correlated nucleotides were independent was less than 0.00001.

The following guidelines were also imposed for nucleotide association analysis and clustering. The average number of modifications detected per read was required to be $\sim 15\%$ of the estimated number of single-stranded nucleotides, yielding an average equal to or greater than two mutations per read. Nucleotides with a mutation rate greater than 0.05 in the no-modification control were excluded from the χ^2 calculation. Correlated nucleotide pairs with a SD of their correlation coefficient (estimated by bootstrapping) greater than 20% were not used as RNA interaction group (RING) constraints. Bootstrapping iterations were sufficiently large so that the absolute difference between bootstrapped and calculated correlation coefficients was less than 1%.

Spectral Clustering of Multiple Conformations in a Single RNA Ensemble. Nucleotides making up an RNA define the dimensions of an abstract high-dimensional space, in which any single read of an RNA strand is represented by a point whose coordinates are defined by which of the nucleotides, if any, reacted with the chemical reagent (each coordinate is set to either 1 or 0, depending on whether the nucleotide that the coordinate represents was reactive or not). In this space, strands with similar structural conformations will tend to cluster, reflecting differences in frequency of modification profiles for each conformation. We used spectral clustering (4–6), which is particularly effective in finding arbitrarily shaped clusters, to define RNA structural clusters, without making any assumptions about the form of the data clusters.

To detect the presence of multiple structural conformations in an RNA pool using spectral clustering, we summarized the locations in the primary sequence (N nucleotides in length) of the nucleotides that were modified by the chemical reagent in M RNA strands, in a “hit” matrix, $H_{M \times N}$. This dataset was treated as a simple, complete, undirected, weighted graph, in which each nucleotide is represented by a vertex with all of the N vertices linked by edges. Each edge was assigned a weight corresponding to the similarity of the reactivity patterns of the two nucleotides, measured as the number of reads in the dataset in which both nucleotides were modified:

$$S = H^T H. \quad [S3]$$

This similarity matrix S was then used to construct a normalized graph Laplacian matrix:

$$L_{NCut} = D^{-1/2} \cdot (D - S) \cdot D^{-1/2}, \quad [S4]$$

where D is a diagonal matrix, in which $D_{ii} = \sum_j S_{ij}$. The eigenvectors of matrix L_{NCut} were used to perform a normalized cut partitioning of the dataset into clusters by cutting the edges between vertices in a way that minimized the sums of the weights of the cut edges and maximized the sum of weights of the preserved edges (4–6). In our application to RNA mutation data, the eigenvalues and eigenvectors of the normalized graph Laplacian matrix L_{NCut} were used to (i) determine how many structural conformations are present in the studied RNA pool, (ii) estimate relative fractions of different conformations in the sample, and (iii) reconstruct mutation frequency profiles for the individual conformations. These procedures are described in detail in the following paragraphs. Spectral clustering was applied to adenosine and cytosine nucleotides that were modified with fre-

quencies greater than 0.01. Strands with no modifications carry no information and were excluded from spectral clustering.

The eigenvalues were sorted in ascending order, from the smallest eigenvalue, λ_1 , to the largest, λ_N . The first eigenvalue, λ_1 , is always zero. Eigenvalues express the effectiveness of each normalized cut partitioning of the vertices. The more effective a particular cut is in cutting edges between dissimilar vertices (such as those belonging to different clusters) while preserving edges between similar vertices (such as those belonging to the same cluster), the smaller its eigenvalue. Therefore, if a dataset has K distinct clusters, the first K eigenvalues will be distinctly smaller than the $K+1$ eigenvalue and the rest of the eigenvalues. Thus, to estimate the number of clusters, K , in a dataset, we chose K such that all eigenvalues $\lambda_2, \lambda_3 \dots \lambda_K$ were relatively small, and λ_{K+1} was relatively large. To make jumps between consecutive eigenvalues more apparent, “eigengaps” (defined as a difference $\Delta\lambda_i = \lambda_{i+1} - \lambda_i$, with the first eigengap, $\Delta\lambda_1$, set to zero) rather than eigenvalues were evaluated (Fig. S9 A and B) (6). In general, if a dataset has K clusters, the eigengap plot will have an outstanding eigengap in the K position ($\Delta\lambda_K$) and also likely to the left of it, but not to the right of it.

Estimating Relative Fractions of Different Conformations in RNA Sample. If a dataset has K clusters, eigenvectors $\vec{x}_2 \dots \vec{x}_K$ can be used to assign individual RNA strands to clusters. Specifically, if a dataset of M strands is recognized to have K clusters, the strand scores are computed as

$$Y_{M \times (K-1)} = H \cdot [\vec{x}_2, \vec{x}_3, \dots, \vec{x}_K], \quad [S5]$$

where $\vec{x}_2, \vec{x}_3 \dots \vec{x}_K$ are the second to the K -th eigenvectors. The scores have $K-1$ dimensions, and the strands are partitioned into K clusters by performing K -means clustering of M data points in the $K-1$ dimensional score space (Fig. S9 C–E).

Reconstructing Modification Frequency Profiles of Individual Conformations in an RNA Sample. Once strands are assigned to clusters reflective of distinct conformations, the modification frequency profiles can be computed specifically for each conformation. The accuracy of such profile reconstruction was improved by computing the modification frequencies of each nucleotide separately using the following procedure. To compute the modification frequencies of nucleotide i , this nucleotide was first removed from the hit matrix H and then spectral clustering and strand partitioning by K -means clustering was performed on this reduced matrix (without the contribution of this nucleotide). Next, the modification frequency of nucleotide i was computed separately for each partitioned group of strands, yielding estimates for different conformations (Fig. S10).

Three-Dimensional RNA Structure Modeling. Three-dimensional RNA fold reconstruction was performed using a restrained molecular dynamics approach in which free energy bonuses were incorporated based on pairwise nucleotide correlations (7, 8). Each nucleotide was modeled as three pseudoatoms corresponding to the phosphate, sugar, and base groups. Pairwise interactions including base pairing, base stacking, packing interactions, and electrostatic repulsion are approximated using square-well potentials (9). Accepted base-pairing arrangements (10–12) were used to constrain modeling.

To incorporate information from RING analysis, free energy potentials were applied during the discrete molecular dynamics (DMD) simulations between nucleotide pairs found to interact. A free energy bonus was included for interacting nucleotide pairs if the absolute correlation coefficient was above 0.025. Free energy potentials were not included if two nucleotides were implicated as being in contact by proximity in primary sequence or

by participation in a common secondary structure element. For primary sequence neighbors, a free energy potential was not included between nucleotides within 11 positions in sequence. For secondary structure neighbors, structural elements were defined as nucleotides at positions n_i and n_j in a RING pair and nucleotides at positions m_i and m_j in any given base pair, if $|n_i - m_j| + |n_j - m_i|$ is less than or equal to 11 nt. The 11-nt threshold was selected based on the number of base pairs in a single turn of an A-form RNA helix.

Free energy potentials were imposed between RING-correlated nucleotide pairs based on through-space distances between constituent nucleotides during simulations. For distances between correlated nucleotides within 36 Å and 23 Å, the applied bonuses were −0.3 and −0.6 kcal/mol, respectively (Fig. S6). The maximum −0.6 kcal/mol bonus is equivalent to stabilization afforded by a single RNA stacking interaction in the molecular dynamics force field.

Molecular dynamics simulations were performed using the DMD engine with replica exchange (13). Eight replicas were run in parallel for 1 million time units each with replica temperature factor values of 0.1000, 0.1375, 0.1750, 0.2125, 0.2500, 0.2875, 0.3250, and 0.3625. From each replica, models at every 100 time

units were taken forward. This list of models was then filtered based on radius of gyration. Radii of gyration for these models were compared against a control simulation where no RING-based potentials were incorporated. For both RING-dependent and control models, radius of gyration histograms were constructed. The control histogram was scaled to minimize its difference from the experimental histogram, and the frequency of the control histogram was then subtracted from the experimental. For this difference histogram, a log-normal distribution was found by least-squares fitting that describes the distribution of radii of gyration for constraint-dependent collapsed structures (Fig. S6D). To be considered further, RING-dependent models had to be within a geometric SD of the geometric mean described by this fit distribution.

Following filtering by radius of gyration, the 250 models with the lowest energies were then analyzed by hierarchical clustering (8). Clustering was performed considering rmsd values between analyzed models. Clustering was constrained such that maximum rmsd between any two constituent members of a cluster was less than the sum of the average and SD of the rmsd distribution predicted for the analyzed structure. The medoid of the most populated cluster was taken as the predicted structure.

1. Wilkinson KA, Merino EJ, Weeks KM (2006) Selective 2'-hydroxyl acylation analyzed by primer extension (SHAPE): Quantitative RNA structure analysis at single nucleotide resolution. *Nat Protoc* 1(3):1610–1616.
2. Siegfried NA, Busan S, Rice GM, Nelson JAE, Weeks KM (2014) RNA motif discovery by SHAPE and mutational profiling (SHAPE-MaP). *Nat Methods* 11:959–965.
3. Yates F (1934) Contingency tables involving small numbers and the χ^2 test. *Supp J Roy Stat Soc* 1:217–235.
4. Shi J, Malik J (2000) Normalized cuts and image segmentation. *IEEE Trans Pattern Anal Mach Intell* 22:888–905.
5. Ng AY, Jordan MI, Weiss Y (2002) On spectral clustering: Analysis and an algorithm. *Advances in Neural Information Processing Systems 14*, eds Dietterich TG, Becker S, Ghahramani Z (MIT Press, Cambridge, MA), pp 849–856.
6. Luxburg von U (2007) A tutorial on spectral clustering. *Stat Comput* 17:395–416.
7. Gherghe CM, Leonard CW, Ding F, Dokholyan NV, Weeks KM (2009) Native-like RNA tertiary structures using a sequence-encoded cleavage agent and refinement by discrete molecular dynamics. *J Am Chem Soc* 131(7):2541–2546.
8. Lavender CA, Ding F, Dokholyan NV, Weeks KM (2010) Robust and generic RNA modeling using inferred constraints: A structure for the hepatitis C virus IRES pseudoknot domain. *Biochemistry* 49(24):4931–4933.
9. Ding F, et al. (2008) Ab initio RNA folding by discrete molecular dynamics: From structure prediction to folding mechanisms. *RNA* 14(6):1164–1173.
10. Serganov A, Polonskaia A, Phan AT, Breaker RR, Patel DJ (2006) Structural basis for gene regulation by a thiamine pyrophosphate-sensing riboswitch. *Nature* 441(7097):1167–1171.
11. Cate JH, et al. (1996) Crystal structure of a group I ribozyme domain: Principles of RNA packing. *Science* 273(5282):1678–1685.
12. Kazantsev AV, Krivenko AA, Pace NR (2009) Mapping metal-binding sites in the catalytic domain of bacterial RNase P RNA. *RNA* 15(2):266–276.
13. Ding F, Lavender CA, Weeks KM, Dokholyan NV (2012) Three-dimensional RNA structure refinement by hydroxyl radical probing. *Nat Methods* 9(6):603–608.

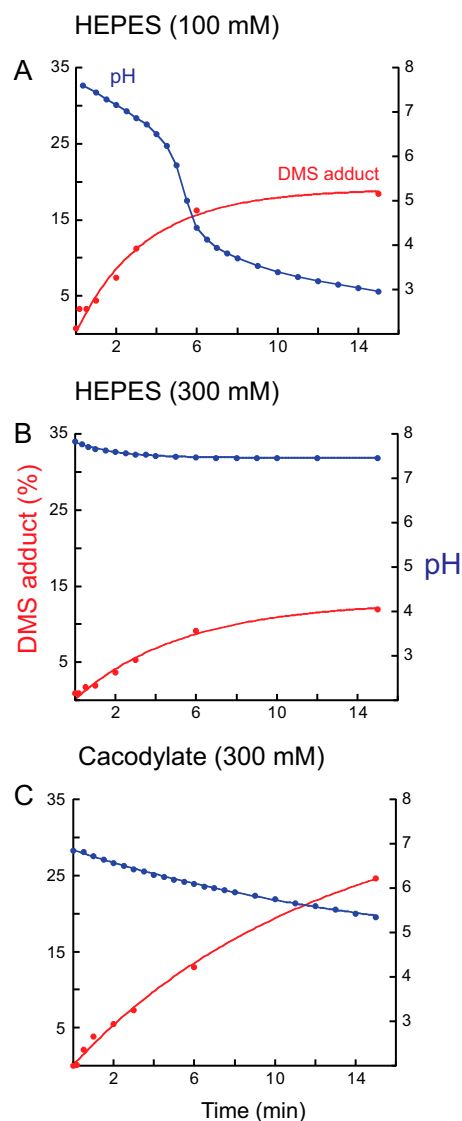


Fig. S1. Optimization of DMS adduct formation. The pH of the DMS reaction (blue lines) and adduct formation with adenosine (red) were monitored as a function of time. The DMS concentration was 170 mM. (A) In 100 mM Hepes (pH 8.0), pH dropped over time, quenching the DMS reaction. These nonideal conditions closely resemble those widely used in conventional DMS experiments. (B) Use of 300 mM Hepes (pH 8.0) as reaction buffer did maintain pH with time; however, the organic buffer reacted directly with DMS, quenching the reaction with adenosine. (C) The pH in reactions performed in 300 mM cacodylate was well-controlled, and the buffer did not react with DMS to quench the reaction.

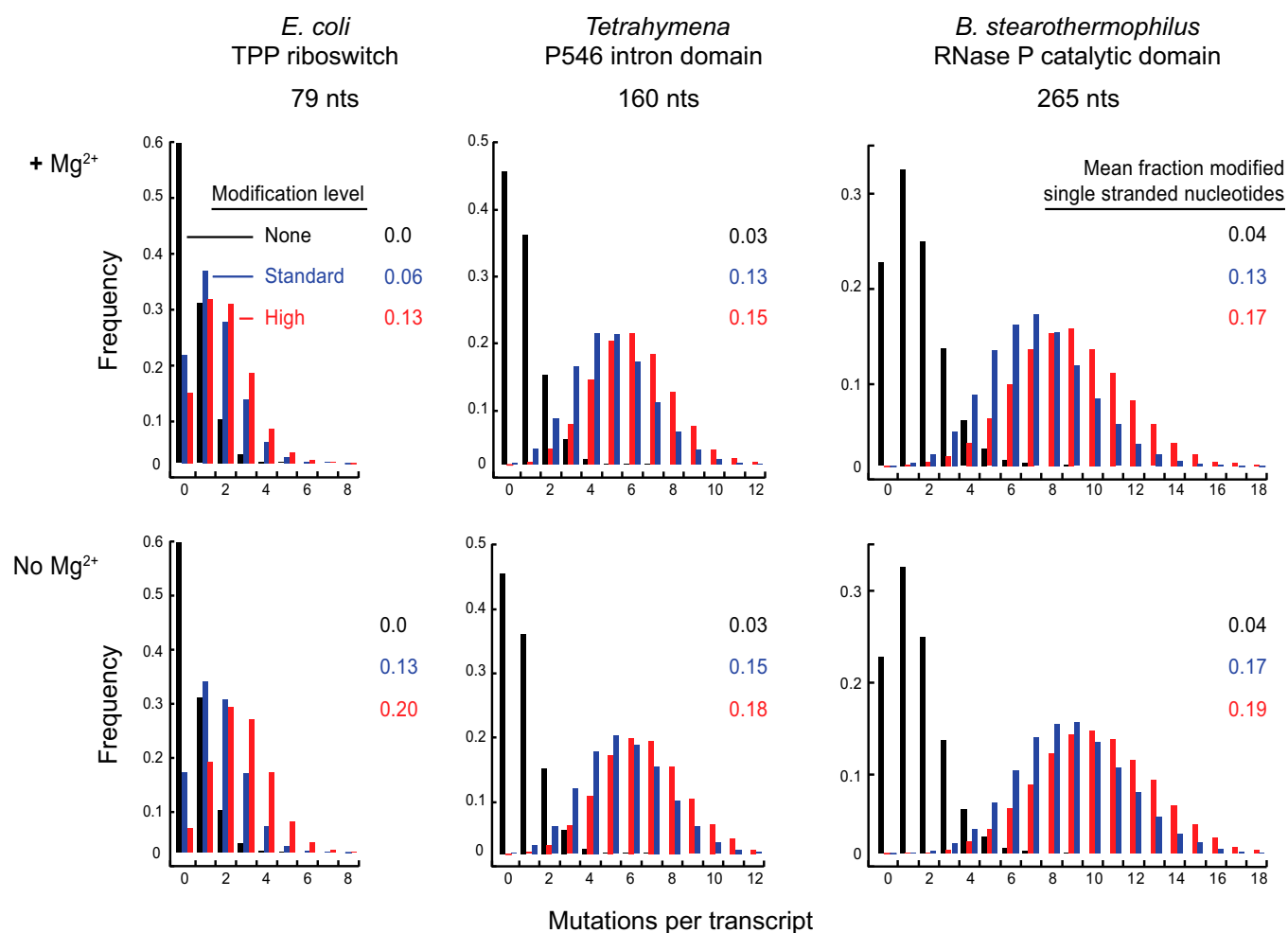
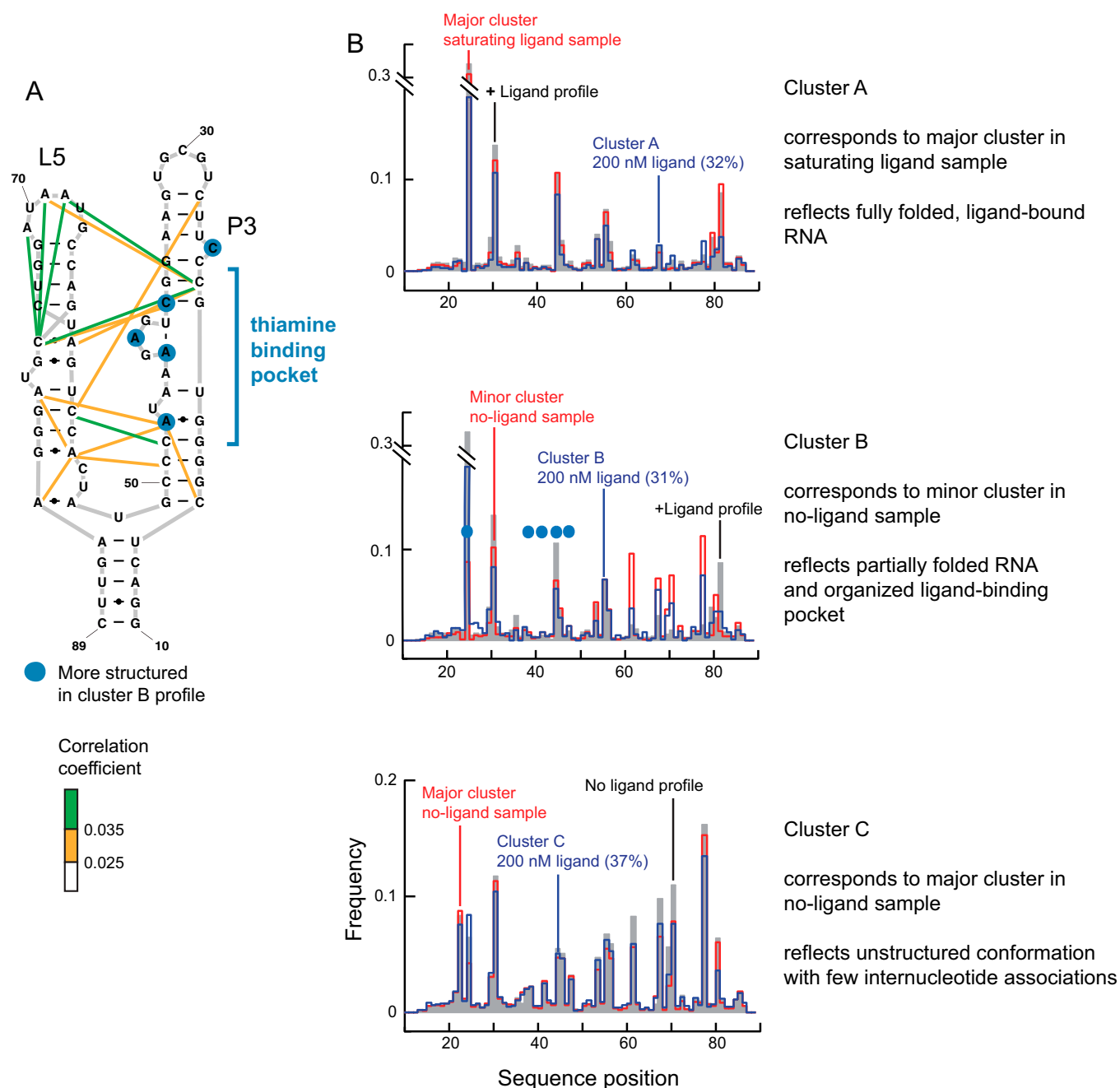


Fig. S2. Effect of modification level and Mg^{2+} concentration on detected mutation level. Distribution of detected mutations for RNAs probed in the presence (Upper) and absence (Lower) of Mg^{2+} and under standard and high level DMS modification conditions (blue and red columns). For experiments with the TPP riboswitch performed in the absence of Mg^{2+} , ligand was also omitted. Standard conditions included 170 mM DMS in 300 mM cacodylate buffer for 6 min; high modification conditions were 250 mM DMS, 750 mM buffer, 15 min.

	Condition	Eigengap	Clusters	Population (%)
TPP	Saturating ligand	0.027 / 0.035	2	75 : 20 : 5*
	No ligand	0.033	2	17 : 83
	No ligand + no Mg ²⁺	0.024	1	—
	200 nM Ligand	0.056 / .044	3	32 : 31: 37
P546 domain J5 mut	Native			
	Mg ²⁺	0.013	1	—
	no Mg ²⁺	0.005	1	—
	P6a mut			
	Mg ²⁺	0.014	1	—
	no Mg ²⁺	0.003	1	—
RNase P				
	Mg ²⁺	0.047	2	76 : 24
	no Mg ²⁺	0.023	1	—

Fig. S3. Summary of spectral clustering analysis for multiple RNA conformations in single ensembles. Clustering analysis is summarized for the TPP riboswitch, P546 domain, P546 mutants, and the RNase P RNA as a function of different levels of structure. The eigengap value measures the structural difference between clusters; samples with eigengaps greater than 0.03 were taken to have two (or more) distinct clusters. The population of each cluster is given in the last column with the most highly structured cluster listed first. An asterisk indicates that smallest cluster population for the TPP riboswitch, at saturating ligand concentration, was too small to accurately generate DMS reactivity profiles. For analysis, the sample was therefore clustered into two conformations with populations of 81% and 19%.



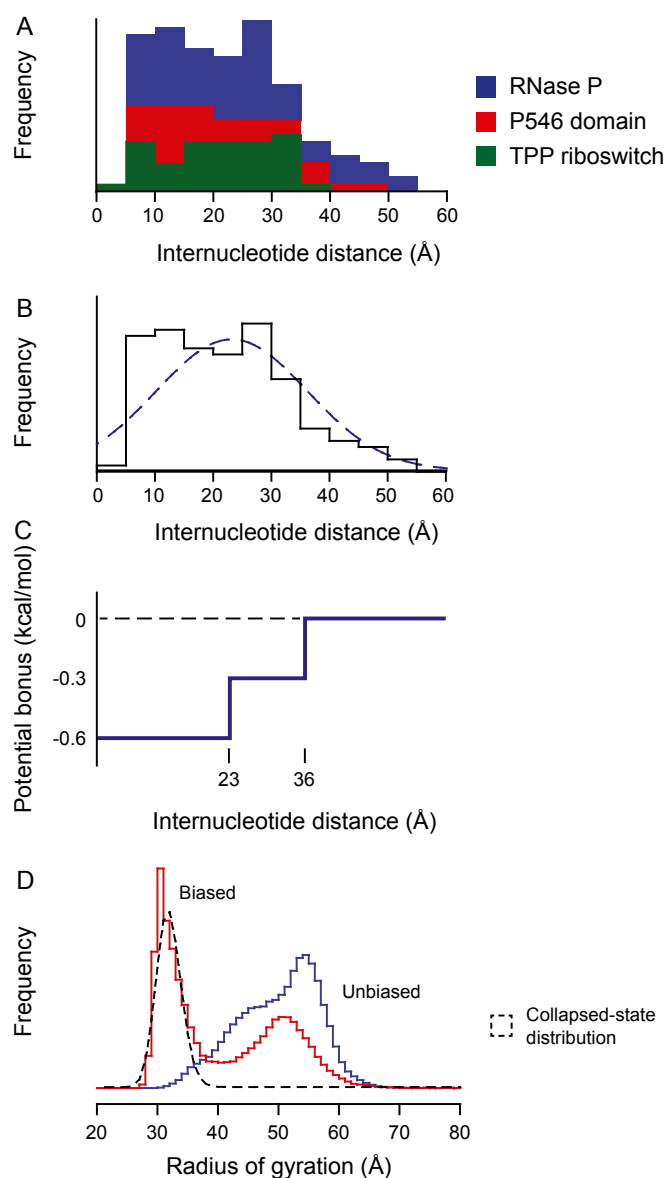


Fig. S6. Long-range constraints for using RING interdependencies to refine 3D RNA structure models. (A) Distribution of distances corresponding to nucleotide associations with correlation coefficients greater than 0.025. (B) Histogram summed over all observations. Smooth curve corresponds to the normal distribution based on the average and SD. (C) Interaction potential for RING-based distance constraints. (D) Radius of gyration-based filtering of structure models. Representative histograms of radii of gyration for models of the P546 domain RNA generated during unbiased simulations (blue) or simulations biased by RING data (red). The fit log-normal distribution for the bias-dependent collapsed state is shown with a dashed line.

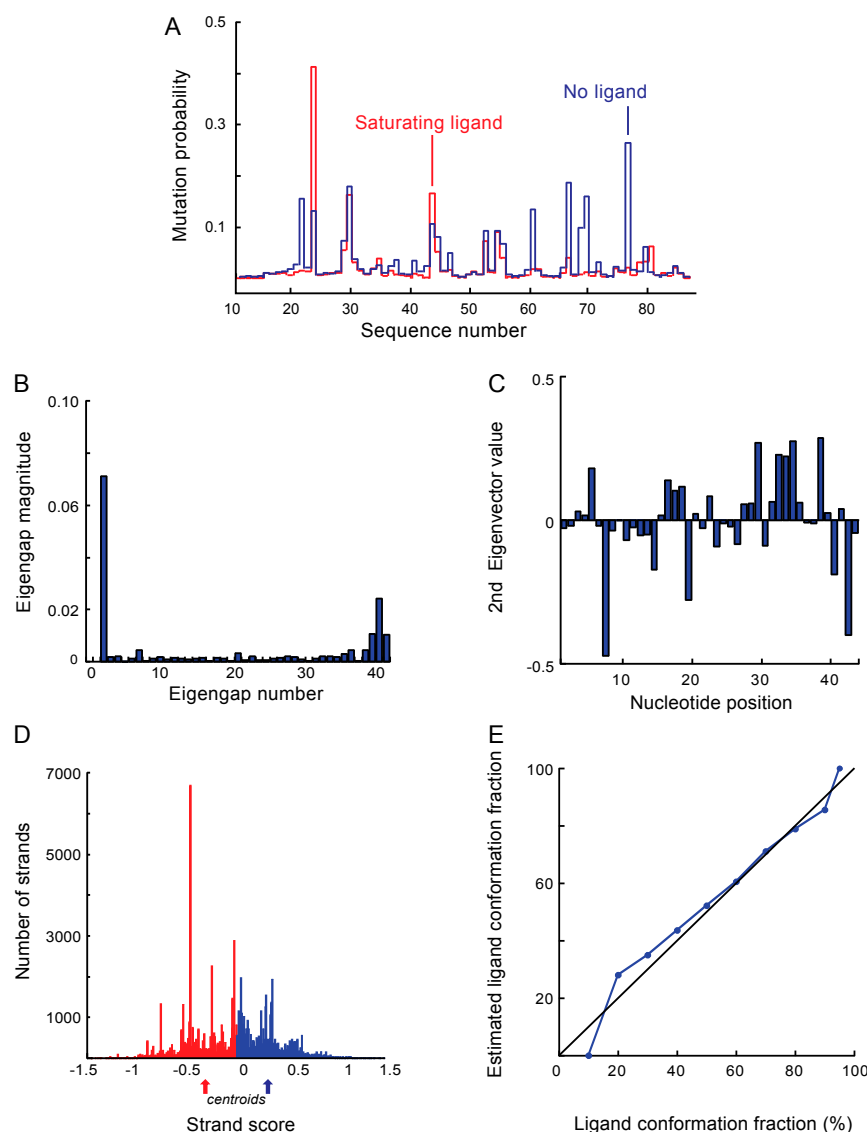


Fig. S9. Spectral clustering of RING-MaP data obtained from analysis of TPP riboswitch RNA. (A) A synthetic data sample of a known conformational composition was created by combining two sets of sequencing reads obtained after modification of the TPP riboswitch RNA: 50,000 reads obtained in the presence of saturating TPP ligand (red) and 50,000 reads obtained in the absence of TPP ligand (blue). Note that these two sets have distinctly different modification frequency profiles, reflecting their different RNA conformations. Any conformational variations that happened to be present within either set were deliberately destroyed by randomly shuffling the recorded instances of nucleotide modifications among the reads. Such shuffling, performed independently for every nucleotide in each set, preserved the total number of modifications to a given nucleotide in a given set but made co-occurrences of modifications among nucleotides statistically random. Thus, this data sample has only two conformations, present at a 1:1 ratio. This synthetic data sample is representative of data collected in single experiments, because nucleotide modifications occur on each strand independently of other strands in the RNA pool. (B) Eigengap plot of the differences in magnitude between successive eigenvalues. Eigenvalues are taken from the normalized graph Laplacian matrix, L_{NCut} , of the similarity matrix, S , constructed for the 43 reactive adenosine and cytosine nucleotides of the synthetic TPP RNA data sample. There is just one outstanding eigengap in this plot, $\Delta\lambda_2$, indicating that the nucleotides form two prominent clusters reflecting two conformations. (C) The second eigenvector, \vec{x}_2 , was chosen to determine the conformational identity of individual RNA strands because the second eigengap indicates that these data are split into two clusters. This eigenvector has 43 values, corresponding to 43 adenosine and cytosine nucleotides with high modification rates. For each nucleotide, the eigenvector magnitude specifies how strongly that nucleotide is associated with either of the two detected clusters. (D) Distribution of the scores for all strands computed from the second eigenvector. The strands that belong to one cluster are on the left side of the score distribution, whereas the strands that belong to the second cluster are on the right side of the distribution. The classification boundary was determined using K -means clustering; red and blue arrows indicate centroids of each cluster. The ratio of strands in the two clusters is 52:48, which is in good agreement with the true ratio of 50:50 for the synthetic dataset. (E) Estimated relative fractions of the ligand-bound and unstructured conformations plotted as a function of their true relative fractions. The plot was generated by performing spectral and K -means clustering on eight different synthetic datasets with different proportions of strands belonging to the two TPP RNA conformations.

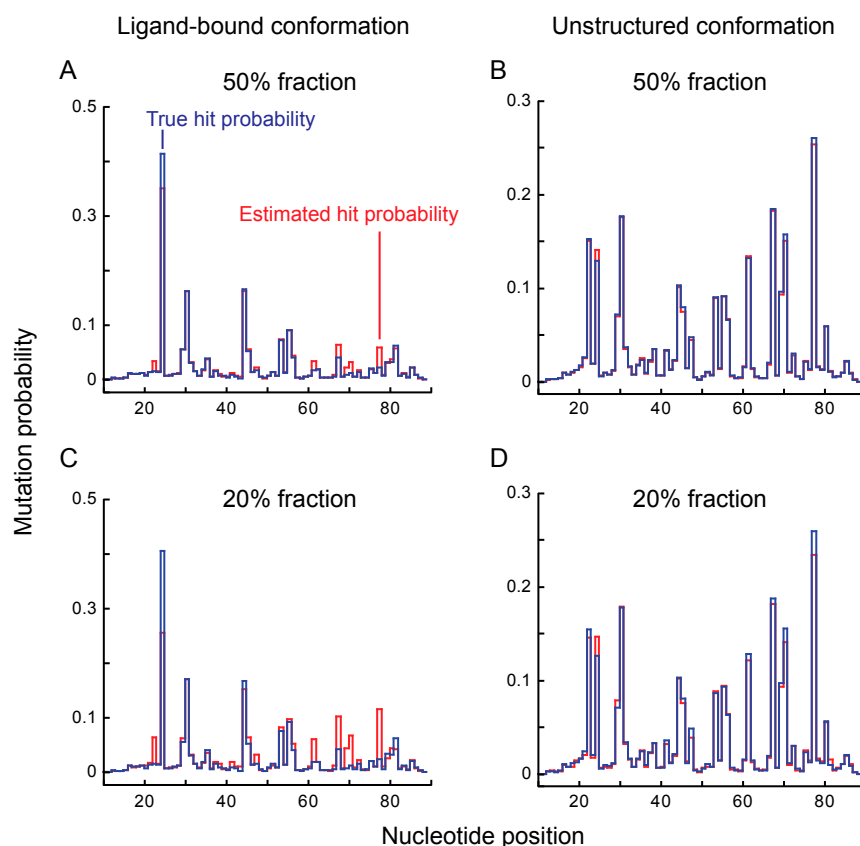


Fig. S10. Reconstruction of mutation probability profiles of individual conformations for data samples containing two conformations each. The two conformations were represented by sequencing reads obtained after modification of the TPP riboswitch RNA in the presence of saturating TPP ligand (ligand-bound conformation) or in the absence of TPP ligand (unstructured conformation), respectively. Any conformational variations within either set were intentionally destroyed by randomly shuffling the recorded instances of nucleotide modifications among the reads (see Fig. S9 legend). To make data samples, the ligand-bound and unconstrained sets of reads were combined at 50:50, 20:80, or 80:20 ratios. (A) The true mutation probability profile (blue) and the profile estimated from spectral and *K*-means clustering (red) for the ligand-bound conformation making up 50% of the data sample. (B) The true and estimated mutation probability profiles for the unstructured conformation making up 50% of the data sample. (C) The true and estimated mutation probability profiles for the ligand-bound conformation making up 20% of the data sample. (D) The true and estimated mutation probability profiles for the unconstrained conformation making up 20% of the data sample. The 80% fractions are not shown because the true and estimated profiles are nearly identical, as expected.